Partitioned MPS-FEM method for free-surface flows interacting with deformable structures

Guanyu Zhang [a], Weiwen Zhao [a], Decheng Wan [a,b,*]

[a] *Computational Marine Hydrodynamics Lab (CMHL), School of Naval Architecture, Ocean and Civil Engineering, Shanghai Jiao Tong University, Shanghai 200240, China*
[b] *Ocean College, Zhejiang University, Zhoushan 316021, China*

ARTICLE INFO

ABSTRACT

In this paper, the partitioned MPS-FEM method is employed for two-dimensional and three-dimensional free surface flow interacting with deformable structures. The discretization of fluid and structure govern equations relies independently on the Moving Particle Semi-implicit method (MPS) and Finite Element Method (FEM). Two types of interpolation techniques, including the Shape Function Based Interpolation Technique (SFBI) and Kernel Function Based Interpolation Technique (KFBI) are proposed on the fluid-structure isomerous interface. The performance of MPS-FEM coupled method is validated by a series of two-dimensional Fluid-Structure Interaction (FSI) tests, including precision test and convergence validation. The results obtained show good agreements with published experimental result as well as referenced numerical results. At last, an extension of aforementioned coupled method to three-dimensional model is performed to investigate characteristics of three-dimensional FSI phenomena. It indicates that partitioned MPS-FEM method is effective and stable for the simulation of free-surface flow interacting with deformable structures.

1. Introduction

The investigations of Fluid-Structure Interaction (FSI) problems are of important significance which appears in many natural phenomena and engineering applications. On the one hand, for the deformable structures under violent hydrodynamic impact, there will be elastic vibration even fatigue damage. On the other hand, the structural response could exert significant influences on the evolution of free surface. Hence, the improvement of computational methods for analyzing FSI problems, especially corresponding to violent free surface flow and deformable structures, is of substantial importance.

A great deal of research has been conducted for fluid interactions with deformable structures using various numerical methods. A well-developed numerical approach is the Arbitrary Lagrangian–Eulerian (ALE) scheme, using Eulerian approach in fluid field and Lagrangian approach in structure field. Kassiotis et al. (2010) calculated violent hydrodynamic pressure that acted on a nonlinear structure through Volume-Of-Fluid (VOF) and Finite Element Method (FEM) coupled strategy. Liao et al. (2015) investigated the phenomenon of free surface flow impacting on an elastic obstacle by experiment as well as numerical simulation based on coupled Finite Difference Method (FDM) and FEM

method. Idelsohn et al. (2008) carried out a series of tests on rolling tank sloshing with an elastic baffle through experiment and numerical simulation. The numerical results based on particle finite element method (PFEM) consist with experimental data. Nevertheless, remeshing is often required for the large movement and deformation of structures in aforementioned schemes, which may introduce an undesired diffusivity, leading to a reduction in robustness and accuracy (Wick, 2013). In the view the characteristics of FSI problems, Lagrangian particle methods, e.g., Smoothed Particle Hydrodynamics (SPH; Lucy, 1977) or Moving Particle Semi-implicit method (MPS; Koshizuka and Oka, 1996) can naturally deal with the large deformations of free surface, together with the moving boundaries. More recently, particle-based methods have been coupled with other methods to model fluid-structure interaction (FSI) problems involving large deformation, such as MPS-FEM (Mitsume et al., 2014; Zhang and Wan, 2019; Zheng et al., 2020a; Zheng et al., 2020b), SPH-FEM (Yang et al., 2012; Fourey et al., 2017; Hermange et al., 2019), MPS-mode superposition method (Sun et al., 2016; Sun et al., 2019a), SPH-Total Lagrangian Particle (SPH-TLP) (Sun et al., 2021; Zhan et al., 2019), ISPH-SPH (Khayyer et al., 2018), multi-resolution MPS-MPS (Khayyer et al., 2019), multi-resolution SPH (Zhang et al., 2021), SPH-smoothed finite element

---

* Corresponding author.
E-mail address: dcwan@sjtu.edu.cn (D. Wan).

method (ES-FEM) (Long et al., 2021), and SPH—Hamiltonian SPH (Khayyer et al., 2021a). In this paper, the MPS-FEM coupled model is applied to investigate the FSI problems, where MPS method is chosen for the simulation of violent free-surface flow of fluids. In addition, FEM has its robustness and accuracy in the solving of structural deformation.

Monolithic approach (Walhorn et al., 2005; Dettmer and Perić, 2007) and partitioned approach (Farhat and Lesoinne, 2000; Tallec and Mouro, 2001) are the common two-way coupling schemes in solving coupled problems. Generally, partitioned approach is more flexible for the complicated FSI problems, since separate governing equations and discrete ways are adopted in both fields. In this study, a weak coupling between FEM and MPS method is implemented, in which the fluid and structure fields are self-governed by different equations. In the partitioned approach, Conventional Serial Staggered (CSS) algorithm and Conventional Parallel Staggered (CPS) algorithm are two alternative partitioned algorithms (Farhat and Lesoinne, 2000). Mitsume et al. (2014) adopted a CSS algorithm as a coupling strategy in MPS-FEM coupled method. The time step adopted in structure solver could be several times of fluid time step. Hermange et al. (2019) improved a CPS algorithm between SPH and FE method for the solution of FSI problems, in which an optimization consisting in authorizing several fluid time steps within each solid one simultaneously evolving is proposed. In present solver, a partitioned coupling of CSS algorithm between MPS and FEM solver is implemented. In the coupled method of MPS-FEM or SPH-FEM, the isomerous interface between the two fields may bring the challenges of data exchange. Therefore, various interpolation techniques have been applied. According to Zhang and Wan (2018), Rao et al., 2017, Rao and Wan, 2018, and Zhang et al. (2019), the solid particles located within the same section are grouped as a node, it is almost no need for the interpolation method. Mitsume et al. (2014) assumes a linear pressure distribution on the boundary side of an element when the pressures are converted into nodal forces. As proposed in Hermange et al. (2019), the external loads applied to the structure field is computed by averaging the fluid pressure. There are also some literatures using particle method coupled with FEM to solve FSI problems with complicated boundary condition. Gao et al. (2021) developed coupled isogeometric analysis (IGA) and least-square MPS (LSMPS) approach for modeling FSI problems with complicated geometries, where the NURBS (Non-Uniform Rational B-Splines) surfaces provide boundary conditions for the LSMPS method. Zheng et al. (2020a; 2020b) proposed ghost cell boundary (GCB) model using FEM to deal with wall boundaries of complicated shapes, and integration points of cells took the place of the cells to achieve the interaction process. In present method, both the shape function in FEM and the kernel function of MPS method have a natural characteristic of interpolation. Therefore, two weight function interpolation techniques based on shape function and kernel function are proposed, called Shape Function Based Interpolation Technique (SFBI) and Kernel Function Based Interpolation Technique (KFBI). In present paper, a more comprehensive and detailed discussion of two data interpolation techniques will be carried out. Compared with the previous papers of our team (Zhang and Wan, 2019; Zhang and Wan, 2018; Rao et al., 2017; Rao and Wan, 2018; Zhang et al., 2019), structural models with more degrees of freedom are applied, which would bring in more challenges in the data interpolation process. What's more, the interpolation techniques can be extended to three-dimensional applications.

The rest of the paper is organized as follows: Section 2 introduces the theories of MPS and FEM briefly. Then, the coupling scheme and interpolation technique at the interface between fluid and structure field are introduced in Section 3. In the Section 4, the structural module and two interpolation techniques are validated firstly through the benchmark tests. After that, a few FSI tests are simulated utilizing the MPS-FEM coupled method. The comparisons between numerical results and experiment data (Antoci et al., 2007; Idelsohn et al., 2008; Liao et al., 2015) are made to validate the accuracy of present method. At last, an extension of aforementioned coupled method to three-dimensional

model is performed to investigate characteristics of three-dimensional FSI phenomena.

2. Numerical method

In this study, partitioned MPS-FEM method is adopted to investigate the FSI problems. The MPS method is used to calculate the fluid field, while the FEM is adopted to solve the structure field. Till now, quite a bit of literatures have focused on improving the stability and accuracy of the projection-based particle method, and some achievements have been obtained, for example, Taylor-series consistent gradient models (Khayyer and Gotoh, 2011; Tamai and Koshizuka, 2014; A. Khayyer et al., 2017a) are used to deal with the unphysical pressure oscillation. Moreover, particle shifting scheme (Lind et al., 2012; Duan et al., 2019; Khayyer et al., 2017b), DS scheme (Tsuruta et al., 2013) and collision model (Lee et al., 2011) are proposed to enhance the stability and accuracy. The MPS model used in this paper follows the existing methods of our team (Zhang and Wan, 2012; Zhang et al., 2014; Tang et al., 2016a; Tang et al., 2016b), which has been proved to be stable and suitable for solving FSI problems through the published literatures.

2.1. MPS formulation for fluid dynamics

The governing equations for viscous incompressible fluid including the continuity equations and the Navier-Stokes equations are expressed in Lagrangian form as following

$$\nabla \cdot \boldsymbol{V} = 0 \tag{1}$$

$$\frac{D\boldsymbol{V}}{Dt} = -\frac{1}{\rho}\nabla P + \nu\nabla^2 \boldsymbol{V} + \boldsymbol{g} \tag{2}$$

where $\boldsymbol{V}$, ρ, P, ν and $\boldsymbol{g}$ denote the velocity vector, the fluid density, the pressure, the kinematic viscosity and the gravitational acceleration, respectively. In particle method, governing equations should be expressed by the particle interaction models based on the kernel function. The kernel function in present paper can be formulated as:

$$W(r) = \begin{cases} \dfrac{r_e}{0.85r + 0.15r_e} - 1 & 0 \le r < r_e \\ 0 & r_e \le r \end{cases} \tag{3}$$

where $r = |\boldsymbol{r}_j - \boldsymbol{r}_i|$ is the distance between particle i and j, and r_e denotes the influence radius of the target particle. Generally, the radius for particle number density and the gradient model is $r_{e\_grad} = 2.1dp$ and it is $r_{e\_lap} = 4.01dp$ for the Laplacian model, where dp is the initial particle space. In MPS, particle interaction models including the gradient, divergence, and Laplacian models are defined as Eq. 4~6.

$$\langle\nabla\phi\rangle_i = \frac{D}{n^0}\sum_{j\neq i}\frac{\phi_j + \phi_i}{|\boldsymbol{r}_j - \boldsymbol{r}_i|^2}(\boldsymbol{r}_j - \boldsymbol{r}_i)\cdot W(|\boldsymbol{r}_j - \boldsymbol{r}_i|) \tag{4}$$

$$\langle\nabla\cdot\boldsymbol{\Phi}\rangle_i = \frac{D}{n^0}\sum_{j\neq i}\frac{(\boldsymbol{\Phi}_j - \boldsymbol{\Phi}_i)\cdot(\boldsymbol{r}_j - \boldsymbol{r}_i)}{|\boldsymbol{r}_j - \boldsymbol{r}_i|^2}W(|\boldsymbol{r}_j - \boldsymbol{r}_i|) \tag{5}$$

$$\langle\nabla^2\phi\rangle_i = \frac{2D}{n^0\lambda}\sum_{j\neq i}(\phi_j - \phi_i)\cdot W(|\boldsymbol{r}_j - \boldsymbol{r}_i|) \tag{6}$$

$$\lambda = \frac{\sum\limits_{j\neq i}W(|\boldsymbol{r}_j - \boldsymbol{r}_i|)\ |\boldsymbol{r}_j - \boldsymbol{r}_i|^2}{\sum\limits_{j\neq i}W(|\boldsymbol{r}_j - \boldsymbol{r}_i|)} \tag{7}$$

where ϕ is an arbitrary scalar function, Φ is an arbitrary vector, D is the number of space dimensions, r is the position vector, λ is a parameter and expressed as Eq. (7), and n^0 is the initial density of the particle number defined as
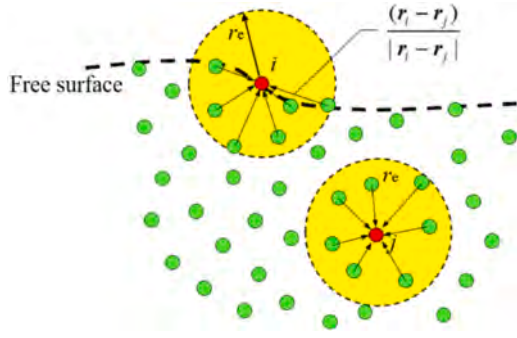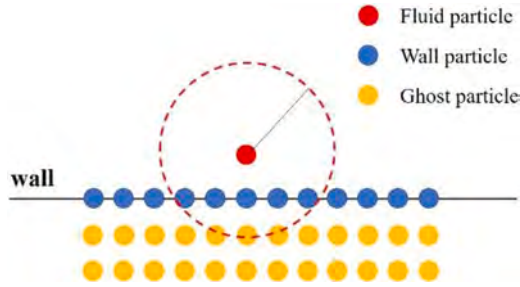
Fig. 1. The detection of free surface particles.

Fig. 2. Schematic of boundary particles.

$$\langle n \rangle_i = \sum_{j \neq i} W\left(\left|r_j - r_i\right|\right) \tag{8}$$

In the present paper, the incompressible condition of MPS method is represented by two parts, the particle number density and the divergence of velocity (Lee et al., 2011; Tanaka and Masunaga, 2010). Pressure is implicitly calculated by solving PPE, and the velocity and position of particles are updated according to the obtained pressure. The PPE in present MPS solver is defined as

$$\left\langle \nabla^2 P^{k+1} \right\rangle_i = (1 - \gamma) \frac{\rho}{\Delta t} \nabla \cdot V_i^* - \gamma \frac{\rho}{\Delta t^2} \frac{<n^k>_i - n^0}{n^0} \tag{9}$$

where γ is the weight of the particle number density term between 0 and 1. The range of $0.01 \leq \gamma \leq 0.05$ is better according to numerical experiments conducted by Lee et al. (2011). In this paper, $\gamma = 0.01$ is adopted for all numerical experiments.

Pressure of the fluid subdomain is closely affected by the accuracy of free surface detection. In the present paper, we employ a free surface detection strategy, shown as in Fig. 1, referred the method by Khayyer et al. (2009) and defined as

$$< F >_i = \frac{D}{n^0} \sum_{j \neq i} \frac{(r_i - r_j)}{|r_i - r_j|} W\left(|r_i - r_j|\right) \tag{10}$$

where F represents the asymmetry of arrangements of neighbor particles. Particles satisfying $< | F |>_i > \alpha | F |^0$ will be considered as a free surface particle, where α is a parameter which has a value of 0.9 in this paper, $|F|^0$ is the initial value of $|F|$ for surface particles.

In MPS method, the boundary condition of free surface is naturally satisfied. For the solid boundary, the treatment of multilayer particles is shown as in Fig. 2. It can ensure a smooth and accurate pressure field around the solid surface and prevent fluid particles from penetrating into the impermeable boundary. The solid boundary is represented by one layer of wall particles. The pressures of these particles and fluid particles are solved by PPE. The function of two layers of ghost particles is to fulfill the particle number density so that the particle interaction can be properly calculated near the solid boundary. The pressures of

these ghost particles are obtained by interpolation.

2.2. FEM formulation for structure dynamics

In the total Lagrangian (TL) formulation (Belytschko et al., 2014), the conservation and momentum equation can be expressed as

$$\rho J = \rho_0 \tag{11}$$

$$\frac{dv}{dt} = \frac{1}{\rho_0} \nabla_0 \cdot P^T + g \tag{12}$$

where P is the first Piola-Kirchhoff stress tensor, subscript 0 means the initial configuration, also called the undeformed configuration, we usually use vector X for the undeformed initial coordinates. While no subscript means the current configuration, and vector x is used for the deformed current configuration. J is used as the determinant of the deformation gradient F, which is defined by

$$F = \frac{dx}{dX} = \frac{du}{dX} + I \tag{13}$$

where u (X, t) is the displacement of material point, given by the difference between the current position and the original position. The Green-Lagrangian strain tensor E is defined by

$$E = \frac{1}{2} \left(F^T F - I \right) = \frac{1}{2} (C - I) \tag{14}$$

where C is the right Cauchy deformation tensor. For linear elastic materials or Kirchhoff materials, P can be obtained by:

$$P = FS \tag{15}$$

where S is the second Piola-Kirchhoff stress tensor, and the constitutive relation between S and strain tensor E can be expressed as:

$$S = C : E \tag{16}$$

in which C is a constant 4th-rank elasticity tensor. For an isotropic elastic solid, the constitutive relation reduces to

$$S = K(\text{tr}E)I + 2G\left(E - \frac{1}{3}(\text{tr}E)I\right) = \lambda(\text{tr}E)I + 2\mu E \tag{17}$$

where $K = \lambda + 2\mu/3$ is the bulk modulus and $G = \mu$ is the shear modulus. λ and μ are Lame's constants, calculated from the Young's modulus, E, and the Poisson's ratio, v. Thus, this fourth-order tensor can be shown as

$$C_{ijkl} = \lambda \delta_{ij} \delta_{kl} + \mu \left(\delta_{ik} \delta_{jl} + \delta_{il} \delta_{jk} \right) \tag{18}$$

where δ_{ij} is the Kronecker deltas or unit matrix: $\delta_{ij} = 1$ if $i = j$, $\delta_{ij} = 0$ if $i \neq j$. The discrete equations for a finite element model are obtained from the principle of virtual work, the momentum equation in TL formulation can be expressed as

$$Ma = f_i^{ext} - f_i^{int} \tag{19}$$

where M is the mass matrix, a is the acceleration of the node, f^{ext} is the common result of the external force and interaction force on the node, and f^{int} is the internal force of the node, which can be defined by:

$$f_i^{int} = K^{mat}u + K^{geo}u \tag{20}$$

where K^{mat} and K^{geo} represent the material tangent stiffness matrix and the geometric stiffness matrix, respectively. K^{mat} and K^{geo} can calculate based on the elasticity tensor and stress tensor. If the damp force cannot be ignored, the resultant discrete governing equation can be written as

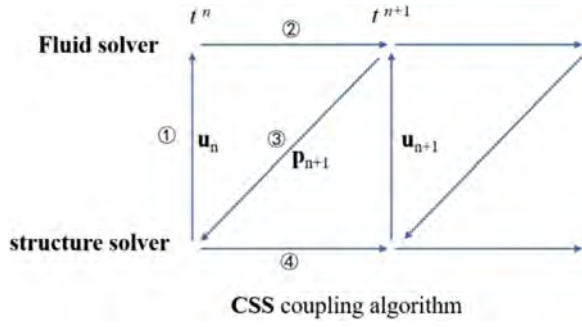$$M \frac{d^2 u}{dt^2} + Ku + C \frac{du}{dt} = F^{ext} \tag{21}$$

Fig. 3. Schematic diagram of partitioned coupling strategy between fluid and structure field.
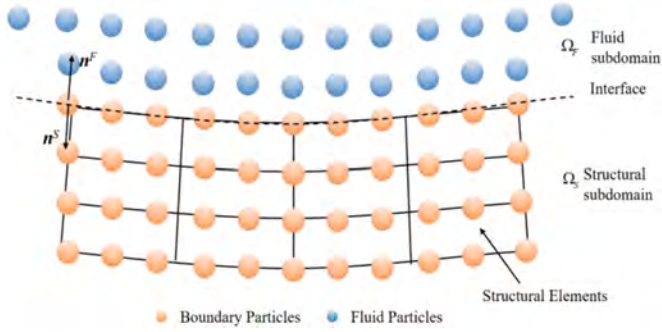

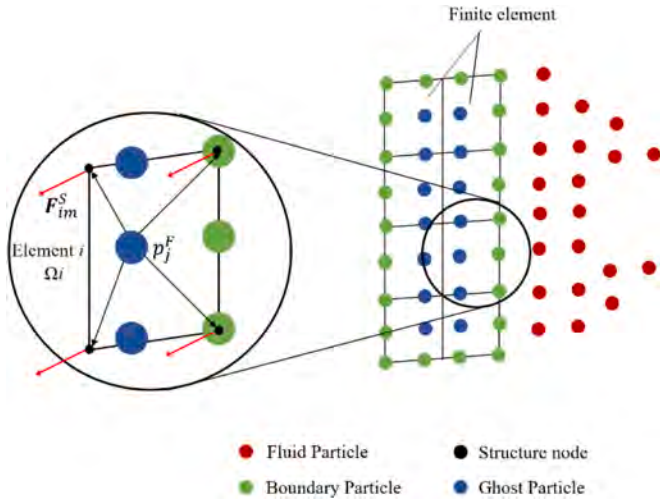**Fig. 4.** Interface between the fluid and structure domain.

Fig. 5. Schematic diagram of the force interpolation based on SFBI.

where $\mathbf{C}$ is the damping matrix. In this study, the Newmark-β method is used to solve the above equation. According to Newmark (1959), the structural node displacement at $t = t+\Delta t$ can be solved with the help of Taylor's expansions of velocity and displacement:

$$\dot{\mathbf{y}}_{t+\Delta t} = \dot{\mathbf{y}}_t + (1-\gamma)\ddot{\mathbf{y}}_t \Delta t + \gamma \ddot{\mathbf{y}}_{t+\Delta t}\Delta t, 0 < \gamma < 1 \tag{22}$$

$$\mathbf{y}_{t+\Delta t} = \mathbf{y}_t + \dot{\mathbf{y}}_t \Delta t + \frac{1-2\beta}{2}\ddot{\mathbf{y}}_t \Delta t^2 + \beta \ddot{\mathbf{y}}_{t+\Delta t}\Delta t^2, 0 < \beta < 1 \tag{23}$$

where β and γ are paramount parameters in the Newmark-β method and are set as β=0.25, γ=0.5 for all simulations. Then the displacement at $t = t+\Delta t$ is proposed by Hsiao et al. (1999)

$$\overline{\mathbf{K}}\mathbf{y}_{t+\Delta t} = \overline{\mathbf{F}}_{t+\Delta t} \tag{24}$$

$$\overline{\mathbf{K}} = \mathbf{K} + a_0\mathbf{M} + a_1\mathbf{C} \tag{25}$$

$$\overline{\mathbf{F}}_{t+\Delta t} = \mathbf{F}_t + \mathbf{M}\left(a_0\mathbf{y}_t + a_2\dot{\mathbf{y}}_t + a_3\ddot{\mathbf{y}}_t\right) + \mathbf{C}\left(a_1\mathbf{y}_t + a_4\dot{\mathbf{y}}_t + a_5\ddot{\mathbf{y}}_t\right) \tag{26}$$

$$a_0 = \frac{1}{\beta\Delta t^2},\ a_1 = \frac{\gamma}{\beta\Delta t},\ a_2 = \frac{1}{\beta\Delta t},\ a_3 = \frac{1}{2\beta}-1,\ a_4 = \frac{\gamma}{\beta}-1,$$
$$a_5 = \frac{\Delta t}{2}\left(\frac{\gamma}{\beta}-2\right),\ a_6 = \Delta t(1-\gamma),\ a_7 = \gamma\Delta t \tag{27}$$

where $\overline{\mathbf{K}}$ and $\overline{\mathbf{F}}$ denote the effective stiffness matrix and effective force vector. Subsequently, the accelerations and velocities related to the next time step are updated as follows:

$$\ddot{\mathbf{y}}_{t+\Delta t} = a_0(\mathbf{y}_{t+\Delta t} - \mathbf{y}_t) - a_2\dot{\mathbf{y}}_t - a_3\ddot{\mathbf{y}}_t \tag{28}$$

$$\dot{\mathbf{y}}_{t+\Delta t} = \dot{\mathbf{y}}_t + a_6\ddot{\mathbf{y}}_t + a_7\ddot{\mathbf{y}}_{t+\Delta t} \tag{29}$$

3. Coupling strategy of partitioned MPS-FEM method

3.1. Coupling algorithm

In present paper, a weak coupling between MPS and FEM method is implemented. The fluid and structure fields are determined separately by their governing equations. Then the Conventional Serial Staggered (CSS) algorithm is applied to realize the communication between MPS and FEM solver, as illuminated in Fig. 3. In the figure, u denotes the structure velocity vector and p represents the fluid pressure, the subscript n stands for the nth time-step. From the figure, it can be seen that the two domains progress alternatively, with the known structural nodal displacement and velocity at the interface at nth time-step, the fluid solver is executed to obtain the velocity field and the pressure field. Then, the hydrodynamic pressure is loaded on the structure. With this external force, new structural nodal displacement and velocity are obtained through the structural solver. The new structural nodal velocities are then transferred to the fluid solver in the next step. In a word, the CSS algorithm is utility for its advantages of flexibility and convenient realization.

3.2. Data interpolation on the fluid-structure interface

On the fluid-structure interface, the interaction is executed by converting the obtained pressures of the boundary particles into equivalent nodal forces, and new structural nodal displacements and velocities are transferred to the boundary particles. It can be noted that the fluid-structure interface boundary conditions are met automatically as follows (Antoci et al., 2007)

$$\mathbf{u}^F = \mathbf{u}^S$$

$$p^F\mathbf{n}^F = -p^S\mathbf{n}^S \tag{30}$$

where $\mathbf{n}^S$ and $\mathbf{n}^F$ are normal vectors to structure and interface boundary particles, as shown in Fig. 4. The superscript F and S represent the physical quantities in the fluid solver and structure solver, respectively. The normal vector of boundary particles $\mathbf{n}^F$ is calculated through the neighbor particles within the effective radius, while the normal vector of structural element $\mathbf{n}^S$ depends on the global coordinate system. By these means, the interface condition of displacement compatibility and traction equilibrium should be met, which indicates the continuity of not only numerical but directional.

In present coupled method, both the shape function in FEM and the kernel function of MPS method have a natural characteristic of interpolation. Therefore, two types of interpolation techniques, including
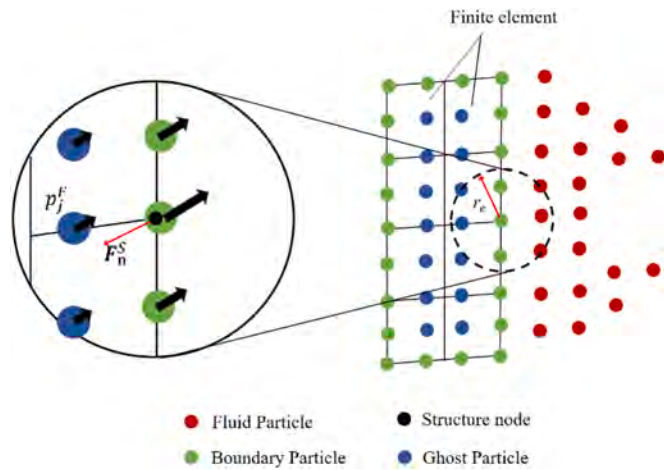
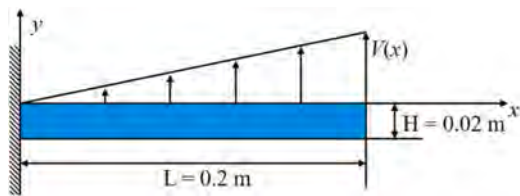**Fig. 6.** Schematic diagram of the force interpolation based on KFBI.

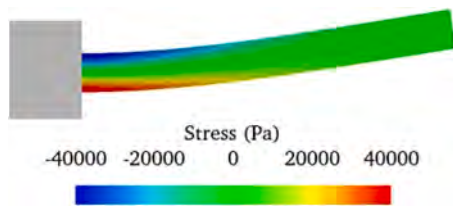

Fig. 7. The geometry of the structure.

Fig. 8. The dynamic response of a free oscillating cantilever plate with stress field at $t = 0.57$ s.
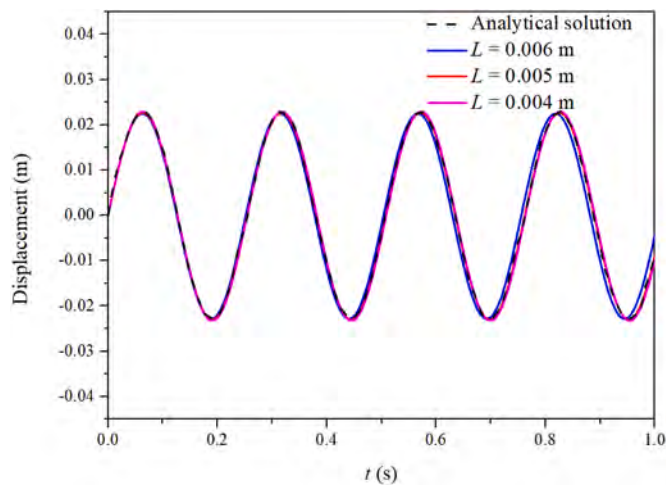

Fig. 9. Time histories of the deflection of cantilever plate with different gird sizes (L).
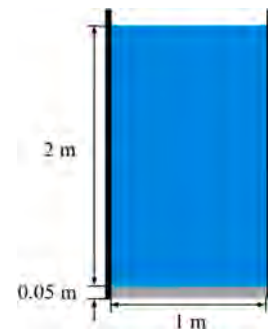

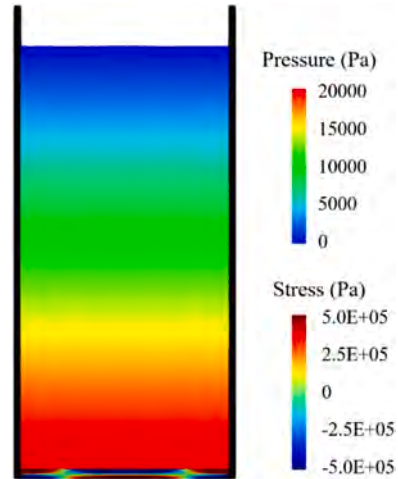**Fig. 10.** Schematic sketch of hydrostatic water column on an elastic plate.

Fig. 11. Snapshot of the pressure and stress fields at $t = 0.5$ s.
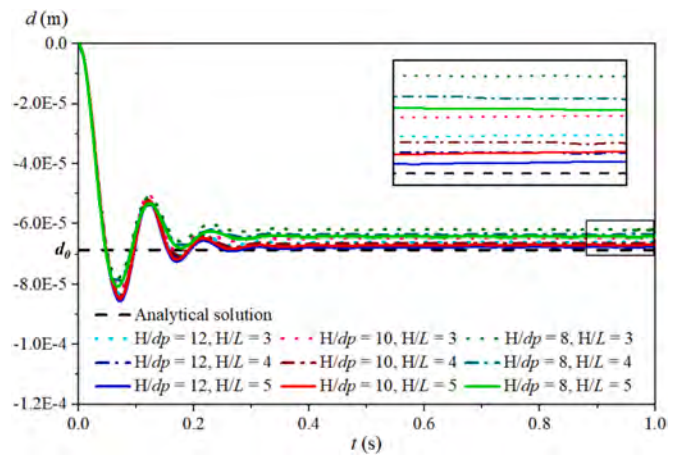
Fig. 12. The time histories of deflection (d) at the plate's mid-span with particle convergence and grid convergence check, compared with the analytical solution.

Table 1

The root-mean-square error (RMSE) of different grid size and effective radius.

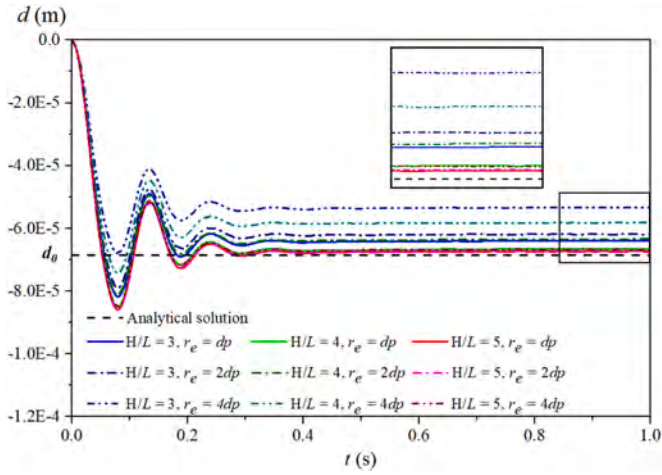| H/dp	H/L = 3	H/L = 4	H/L = 5
8	6.5246E-6	4.97498E-6	4.28562E-6
10	3.85667E-6	2.15379E-6	1.51129E-6
12	2.55753E-6	1.4896E-6	8.41851E-7

Fig. 13. The time histories of deflection (*d*) at the plate's mid-span with grid convergence and effective radius check.

Table 2
The computational error of different grid size and effective radius.

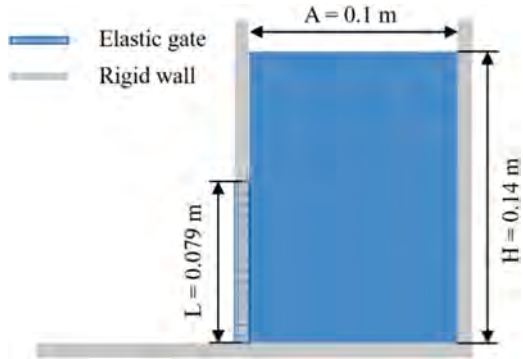| H/L	H/LError	SFBI	KFBI		
			$r_e = dp$	$r_e = 2dp$	$r_e = 4dp$
3	FIE	0.9515	0.8964	0.8770	0.8271
	RMSE	3.85667E-6	4.45135E-6	6.53931E-6	1.50177E-5
4	FIE	0.9525	0.9541	0.9403	0.8789
	RMSE	2.15379E-6	1.78825E-6	4.87618E-6	1.01918E-5
5	FIE	0.9567	0.9624	0.9563	0.9469
	RMSE	1.51129E-6	1.08374E-6	1.23371E-6	1.73424E-6

Fig. 14. Schematic view of dam-break flow with elastic gate.

Shape Function Based Interpolation Technique (SFBI) and Kernel Function Based Interpolation Technique (KFBI) are proposed.

According to the SFBI, shown as Fig. 5, for an element *i* with space Ω_i, the nodal force F^S_{im} of node *m* can be computed as follow

$$\boldsymbol{F}^S_{im} = \sum_{j \in \Omega_i} p^F_j \cdot \boldsymbol{n}^F_j \cdot l_0 \cdot N^j_m \tag{31}$$

where subscript *j* means the boundary particle within the element *i*, but not the ghost particles. N^j_m stands for the shape function value of the node *m* at the particle *j*. p^F_j denotes the hydrodynamic pressure of boundary particle *j* obtained by PPE. $\boldsymbol{n}_j$ is the normal vector corresponding to the boundary particle *j*. *dp* stands for the initial particle spacing. Then the particle position can be updated by the interpolation based on the current structural velocity, as follow
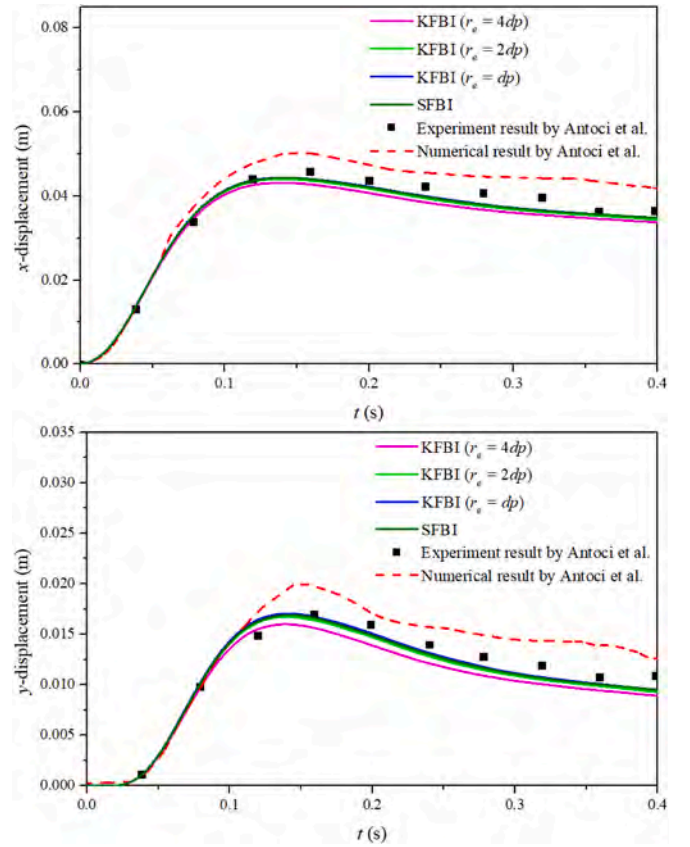

Fig. 15. Horizontal and vertical displacements of free end of gate.

Table 3
The computational error of different grid size and effective radius.

L=dp	SFBI	KFBI		
		$r_e = 4dp$	$r_e = 2dp$	$r_e = dp$
ε (%)	3.803	5.096	4.102	3.234

$$\boldsymbol{w}^F_j = \sum_{m \in \Omega_i} \boldsymbol{\delta}_m \cdot N^j_m \tag{32}$$

where $\boldsymbol{w}^F_j$ is the displacement of boundary particle *j*. δ_m denotes the displacement of node *m*.

According to the KFBI, shown as Fig. 6, the structure particle *i* will be denoted as a neighbor particle of the node while the distance between the particle and the node is smaller than the effective radius r_e. Then, the equivalent nodal hydrodynamic pressure p^s_n is estimated by the weighted value of force components regarding to the neighbor particles, which is defined by

$$p^s_n = \frac{\sum_i p^F_i \cdot \boldsymbol{n}^F_i \cdot W(|\boldsymbol{r}_i - \boldsymbol{r}_n|)}{\sum_i W(|\boldsymbol{r}_i - \boldsymbol{r}_n|)} \tag{33}$$

The displacement of boundary particles is calculated by neighbor nodal displacement when the distance between the particle and the node is smaller than the effective radius r_e. Then particles' displacement can be obtained by the interpolation based on the kernel functions $W(|\boldsymbol{r}_i - \boldsymbol{r}_m|)$, the nodal displacement δ_i.

$$\boldsymbol{w}^F_m = \frac{\sum_i \boldsymbol{\delta}_i \cdot W(|\boldsymbol{r}_i - \boldsymbol{r}_m|)}{\sum_i W(|\boldsymbol{r}_i - \boldsymbol{r}_m|)} \tag{34}$$

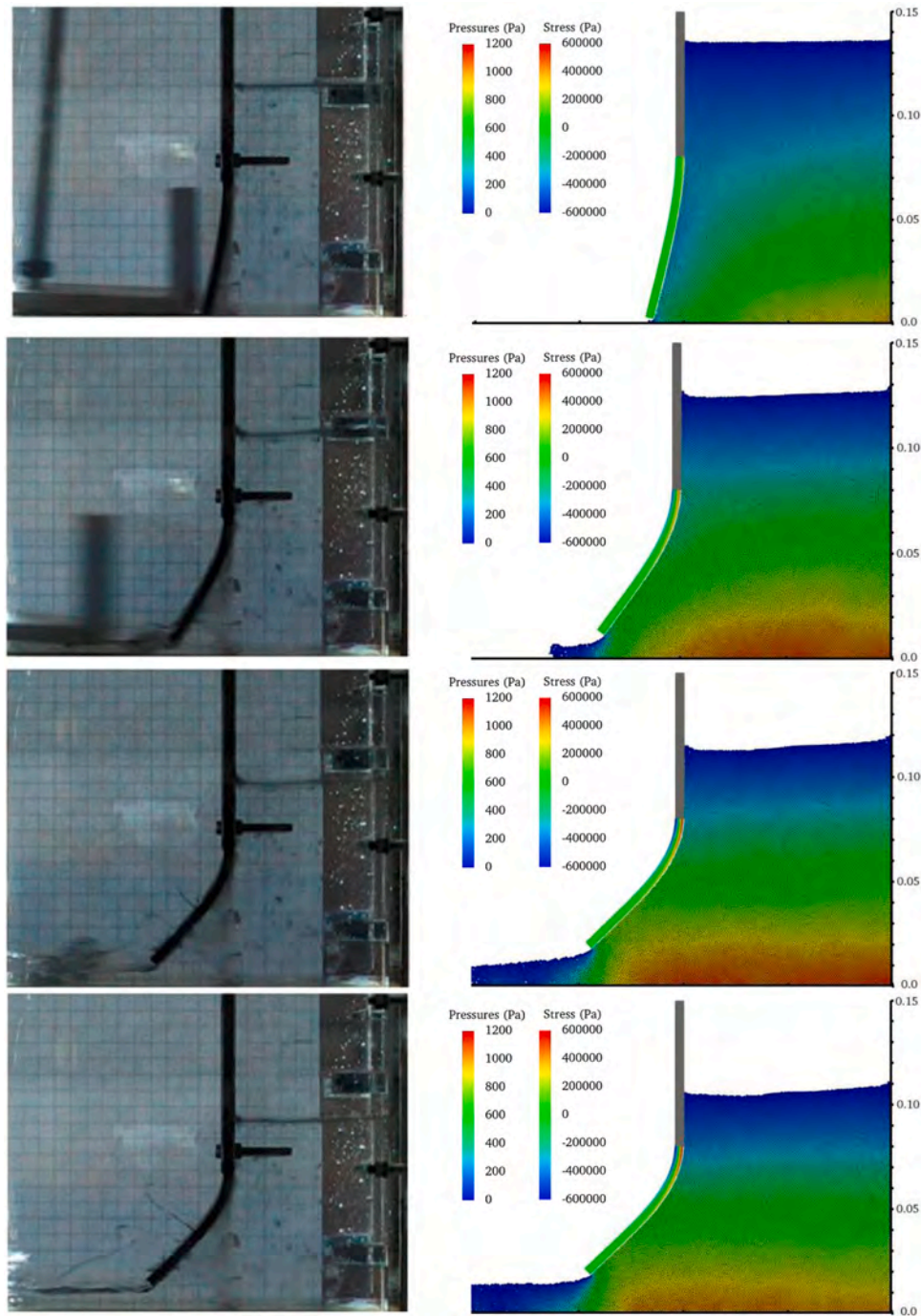It should be noted that, the effective radius r_e in the interpolation

Fig. 16. Snapshots of structural deformation and free surface. ($t = 0.04$ s, 0.08 s, 0.12 s, and 0.16 s, respectively).

scheme does not mean the effective radius for the gradient model or Laplacian model. Generally, the size of grid in the structure solver is one of the most important influence factors of SFBI or KFBI. However, by means of KFBI, the effective radius r_e also has effect on the interpolation accuracy. In the next section, the efficiency and accuracy of above two interpolation technique is validation.

4. Numerical simulation

In this section, the accuracy of present solver in the two-dimensional structural response analysis and the interpolation technique is verified at first. Then, a series of tests are simulated to verify the applicability of the MPS-FEM coupled method in two-dimensional FSI problems,

including dam break with an elastic gate (Antoci et al., 2007), the tank sloshing interacting with an elastic baffle (Idelsohn et al., 2008) and dam-break flow impacting onto an elastic obstacle (Liao et al., 2015), the obtained numerical results will be compared with experimental and numerical result. In the end, the present method is extended to a 3D FSI test.

4.1. Validation of the structural module

To validate the accuracy of present structural solver, response of the cantilever plate under an initial velocity is studied (Landau and Lifshitz, 1970; Gray et al., 2001). The sketches of plate geometry and load history are shown as Fig. 7. The cantilever plate with a total free span length of
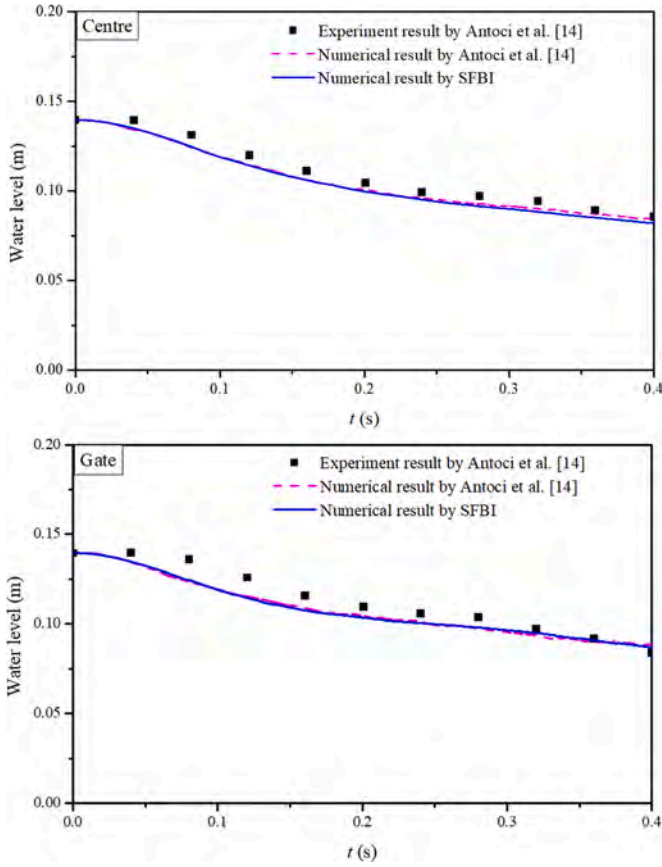
Fig. 17. Water level just behind the gate and 5 cm far from it.

$L = 0.2$ m and thickness of $H = 0.02$ m is dispersed into plane elements. The plate is subjected to an initial velocity distribution of $v_y(x)$, perpendicular to the axis of plate as

$$V_y(x) = V_0 C_0 \frac{f(x)}{f(l)}$$

$$f(x) = (\cos kL + \cosh kL)(\cosh kx - \cos kx) + (\sin kL - \sinh kL)(\sinh kx - \sin kx) \qquad (35)$$

where, C_0 represents the speed of sound, set as

$$C_0 = \sqrt{\frac{E}{2(1 - 2\mu) * \rho_s}} \qquad (36)$$

and E, μ and ρ_s are the Young's modulus, Poisson's ratio and density of elastic plate as 2×10^6 Pa, 0.4 and 1000 kg/m³, respectively; V_0 is velocity amplification factor, which is set as 0.001 in this case. Also, since the fundamental mode of vibration is considered, $kL = 1.875$ (k is the wave number). What's more, the simulation is conducted with three kinds of different grid sizes, 0.004, 0.005 and 0.006 m, to check the convergence property of the FEM structure module.

Fig. 8 shows the snapshot of stress field of dynamic response of plate by present structure solver at $t = 0.57$ s under middle gird size. It is noted that the structure model has provided stable and smooth stress field. The time history of deflection of free end of the cantilever plate, obtained by present structure module with different grid sizes is shown in Fig. 9. According to the comparison between present results and analytical solution, the reproduced structural response can be achieved, and obtained results show that the present structure solver has good convergence. Therefore, present structure solver using FEM is suitable and accurate in solving structural deformation.

4.2. Validation of interpolation technique

In this section, the coupling algorithm accuracy of the interfacial data transformation is validated. A benchmark test of hydrostatic water column on a thin deformable plate (Fourey et al., 2017) is reproduced by the MPS-FEM coupled method. Fig. 10 shows a schematic sketch of this

Table 4
The computational parameters.

Fluid Parameters	Case1	Case2
Fluid density (kg/m³)	917	917
Kinematic viscosity (m²/s)	5×10^{-5}	5×10^{-5}
Fluid depth (mm)	57.4	114.8
Rolling frequency (Hz)	0.61	0.83
Rolling amplitude (degree)	4	4
Initial particle spacing (m)	0.001	0.001
Total numbers	34,428	68,856
Time size in fluid domain (s)	1×10^{-4}	1×10^{-4}
Structure Parameters	**Case1**	**Case2**
Structure density (kg/m³)	1100	1100
Young's modulus (MPa)	6	6
Length (mm)	57.4	114.8
Width (mm)	4	4
Initial element numbers	4×25	4×40
Time size in structure domain (s)	2×10^{-3}	2×10^{-3}
Interpolation technique	SFBI	SFBI

Case1. Elastic beam interacting with shallow water flow

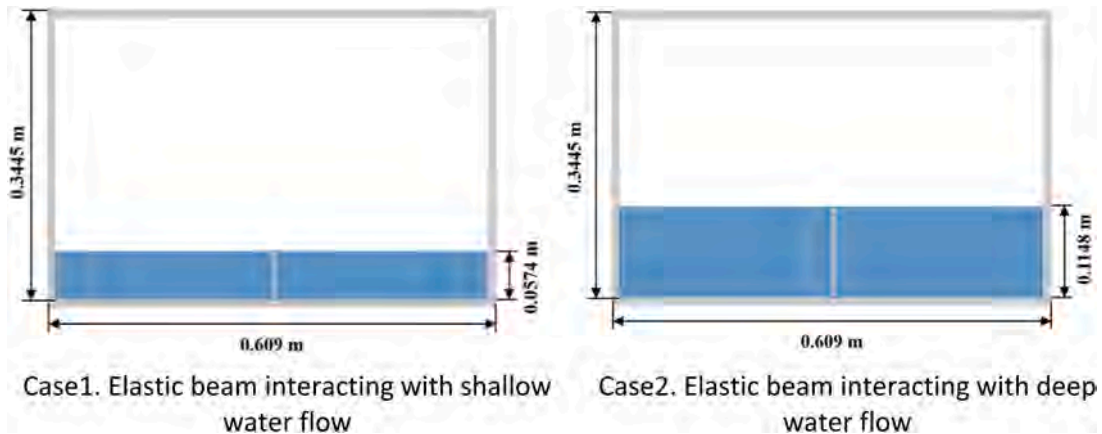Case2. Elastic beam interacting with deep water flow
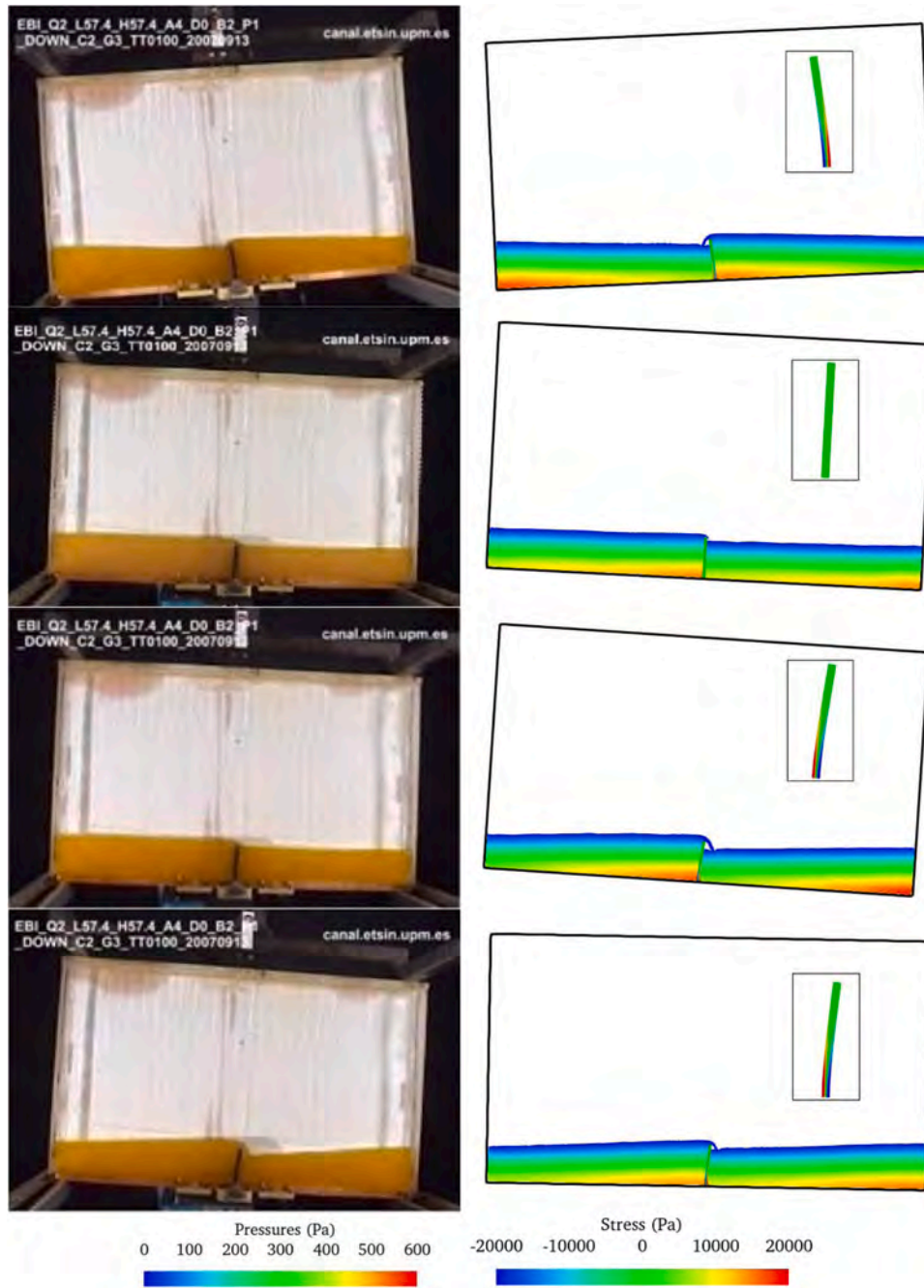
Fig. 18. Sketches of the rolling tank with elastic beams.

Fig. 19. Deformation of baffle and elevation of free surface for Case 1, $t = 0.95, 1.35, 1.62,$ and 1.88 s.

benchmark test. The hydrostatic pressure load of a water column of 2 m height suddenly subjected on the plate, which eventually reaches out an equilibrium state with a constant deformation. The thick (H), density, Young's modulus and Poisson's ratio of plate are 0.05 m, 2700 kg/m^3, 67.5 GPa and 0.34, respectively. To stabilize the deformation as soon as possible, the damping effect is not ignored here. According to the theoretical solution, the magnitude of static deformation at the mid-span of plate under the hydrostatic pressure loading of 2 m high water column would be $d_0 = -6.85$E-5 m.

Fig. 11 presents the pressure and stress fields of hydrostatic water column on an elastic plate at $t = 0.5$ s. The numerical conditions for the corresponding simulation are H/$dp = 10$, H/$L = 4$ and SFBI is used. It can be seen that the pressure/stress field is quite smooth. In addition, particle convergence and grid convergence study are conducted, to investigate the stability and accuracy of two interpolation techniques,

SFBI and KFBI. From Fig. 12, the particle resolution is from H/$dp = 8$ to H/$dp = 12$ and the mesh resolution is from H/$L = 3$ to H/$L = 5$, where SFBI is used for interfacial data interpolation. It can be seen that the deformation will eventually reach a stable status, and the calculated static deformations are all slightly smaller than the theoretical static displacement. However, it would converge to the analytical solution with the particle resolution of H/$dp = 10$ or 12 and the mesh resolution of H/$L = 4$ or 5. Table 1 presents the root-mean-square error (RMSE) corresponding to numerical results shown in Fig. 12, where RMSE can be expressed as,

$$RMSE = \sqrt{\frac{1}{n}\sum_{i=1}^{n}(d(t)-d_0)^2} \qquad (37)$$

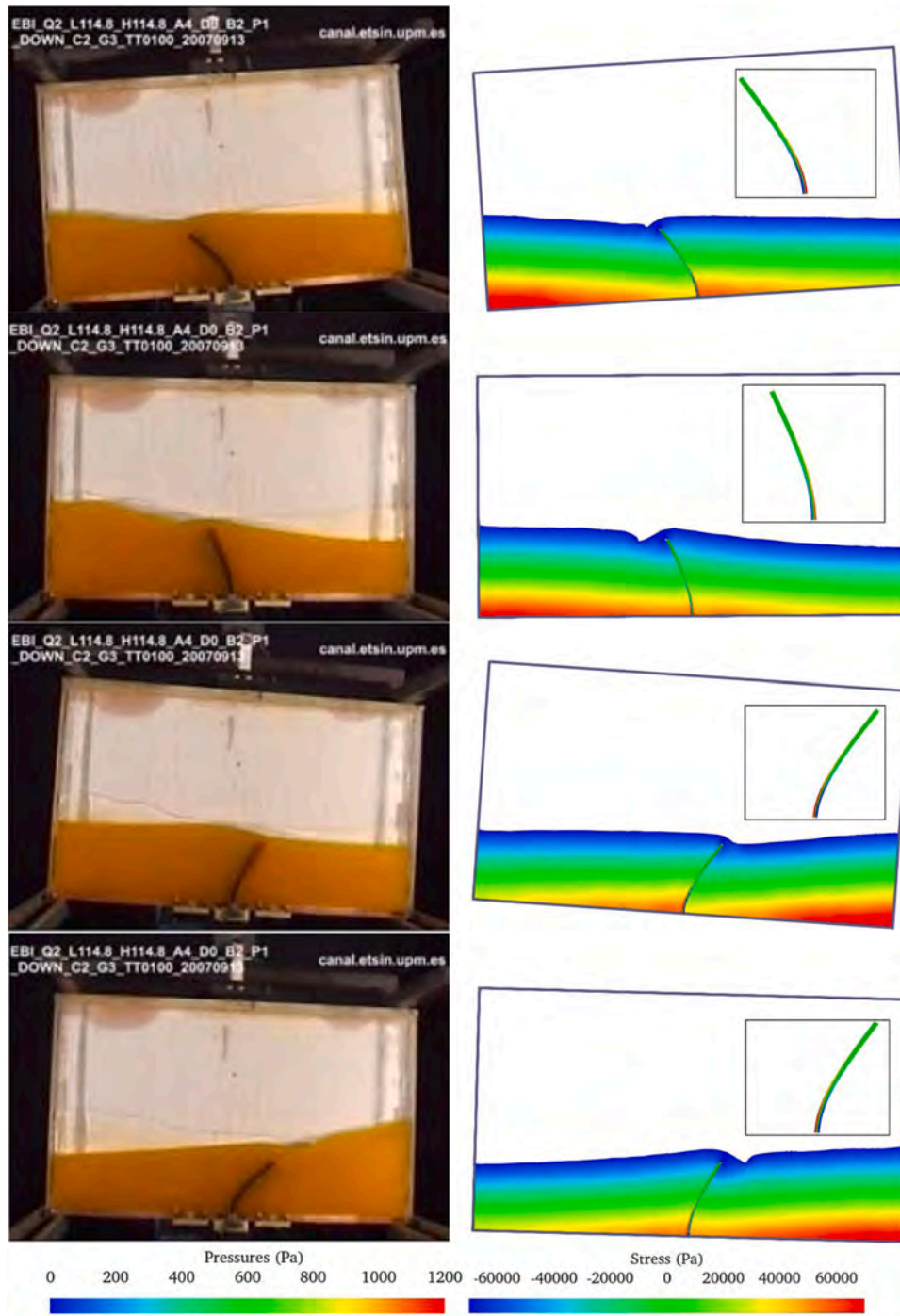Through the comparison, it can be found that the interpolation

Fig. 20. Deformation of baffle and elevation of free surface for Case 2, $t = 1.84, 2.12, 2.32, 2.56$ s.

accuracy of SFBI under different gird sizes is fairly same, the error is relatively small. The MPS-FEM coupled method with the data interpolation technique of SFBI has advancements such as high precision and good convergence.

With regard to the data interpolation technique of KBFI, the interpolation accuracy is affected by the grid size L and the effective radius r_e. To validate the effectiveness of KFBI, the simulation with particle resolution of $H/dp = 10$, the mesh resolution from $H/L = 3$ to $H/L = 5$ and effective radius from $r_e = dp$ to $r_e = 4dp$ is conducted, as shown in Fig. 13. It can be seen that the numerical result through KFBI is same to the result by SFBI, the deformation will eventually reach a stable status, and the deformations are all slightly smaller than the theoretical displacement.

When the finest gird ($H/L = 5$) is chosen, the numerical result presents good agreement with the theoretical displacement under each effective radius. When effective radius r_e is large ($r_e = 4dp$), the numerical result is always relative smaller. When effective radius r_e equals dp, the numerical result has a better approximation to the theoretical solution. In order to analysis the reason, Table 2 presents the RMSE corresponding to the static deformations shown in Fig. 13, and the force interpolation error (FIE), which denotes the ratio of the summation of node force to hydrostatic pressure. It can be found that the accuracy of the numerical result is related to the force interpolation accuracy. The interpolation accuracy of SFBI under different gird sizes is fairly same, the error is relatively small. In contrast, the method with the data interpolation
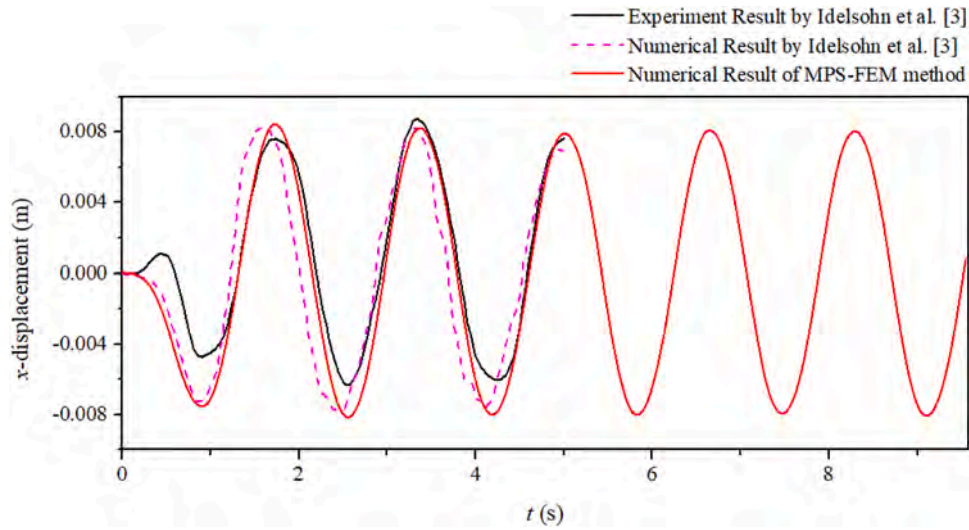
Fig. 21. Comparison of the horizontal displacement of the top of baffle (Case1).
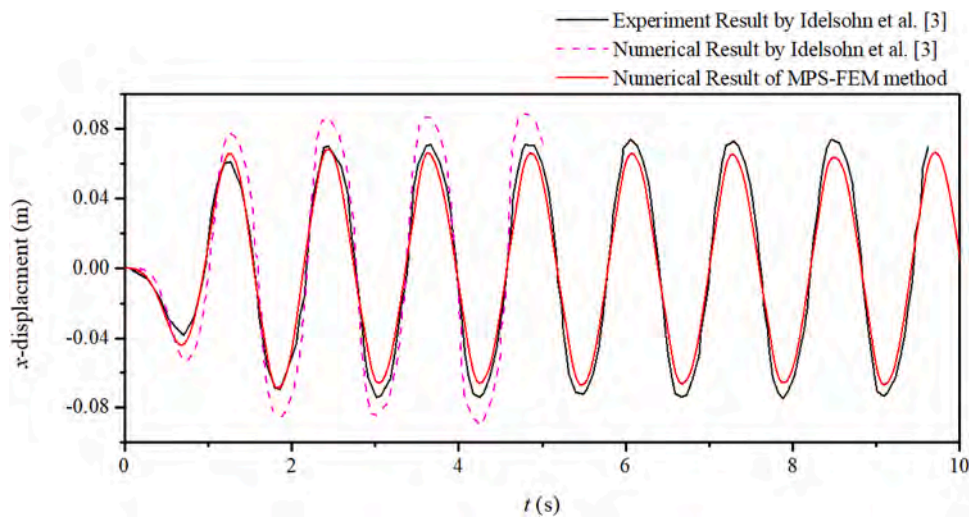

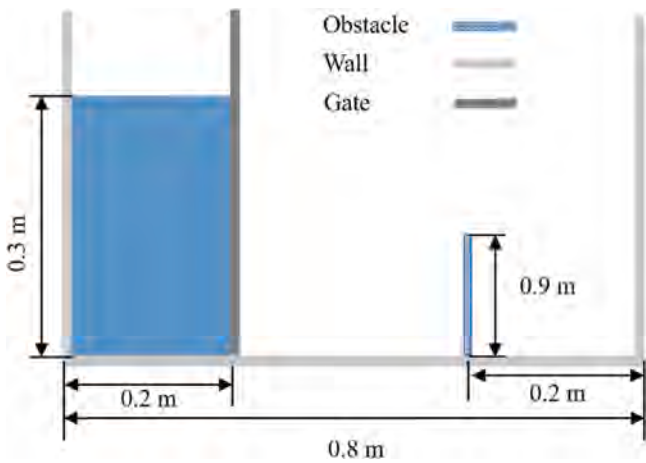**Fig. 22.** Comparison of the horizontal displacement of the top of baffle (Case2).

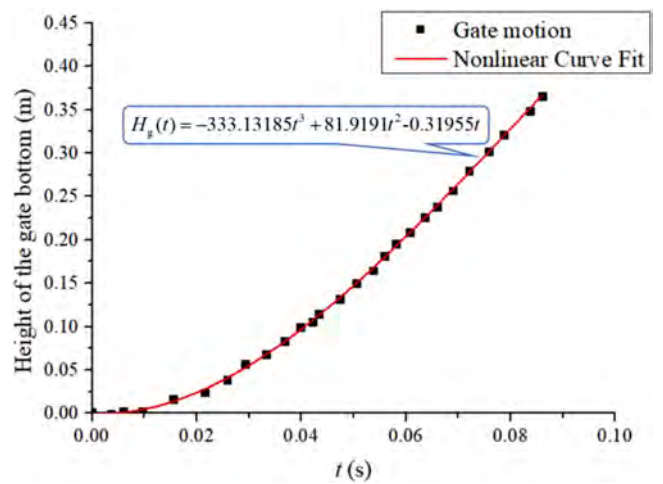**Fig. 23.** Schematic view of dam-break impacting with an elastic obstacle.

$H_g(t) = -333.13185t^3 + 81.9191t^2 - 0.31955t$

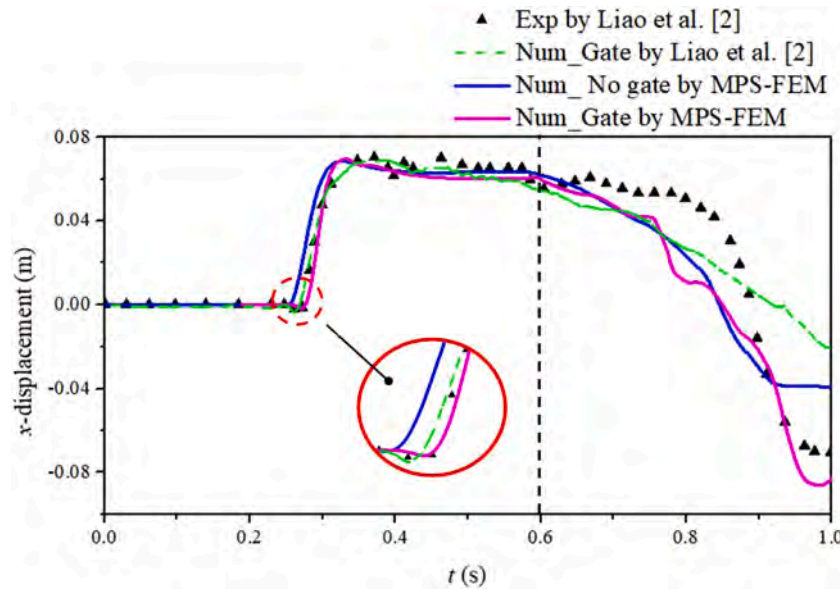**Fig. 24.** The gate motion compared with the experiment.

Fig. 25. The *x*-direction deformation of free end of elastic obstacle.

technique of KFBI has the problems such as nonstability and slow convergence. However, if the effective radius is chosen more cautiously, it could obtain more accurate results with the interpolation technique of KFBI than the interpolation technique of SFBI. By comparison, it can be found that the data interpolation technique of SFBI is better with its stability and robustness, while the data interpolation technique of KFBI is better with its accuracy. The likely cause may be that the realistic fluid-structure interface differs from the treatment of multilayer boundary particles, which may interfere with the force interpolation accuracy through KFBI. When the gird size and effective radius are selected appropriately, the influence of ghost particles on the interpolation process can be avoided.

4.3. Dam-break flow through an elastic gate

The first FSI test for the present coupled method is a case of the dam-break flow through an elastic gate, which was published by Antoci et al. (2007), the obtained numerical result is compared with experimental and numerical data. The initial configuration is illustrated in Fig. 14. The elastic gate is of 0.005 m thickness and 0.079 m length with the density and Poisson's ratio of 1100 kg/m^3 and 0.4. Due to the linear constitutive model applied in this paper, the Young's modulus of the elastic gate is 10 MPa, which is relatively smaller than the experiment. The fluid partition consists of water with density of $\rho = 1000$ kg/m^3 and kinematic viscosity of $\nu = 1.01 \times 10^{-6}$ m^2/s. The initial particle spacing is set as $dp = 0.001$ m. As for the structure domain, the structural damping is assumed negligible compared to inertial forces. In this test, the efficiency and accuracy of above two interpolation techniques are in validation once again. The gird size is set as $L = dp$ and the effective radius is chosen to $r_e = dp$, $2\,dp$, $4dp$, respectively.

Horizontal and vertical displacements of free end of gate are shown in the Fig. 15 versus the experiment result and numerical result from Antoci et al. (2007). From the figure, it can be observed that the numerical results obtained by two interpolation techniques present good agreement with the experiment result. Specially, when the value of effective radius r_e is more centered, the numerical result has a better approximation to the experiment result. In order to more visually observe and compare two interpolation techniques, the error in quantitative between experimental data and numerical result is shown in Table 3. It can be found that the accuracy of KFBI is greatly affected by the effective radius. By comparison, the conclusion obtained is approximate to the test of hydrostatic water column on a deformable

plate. In the following numerical simulation, SFBI is the only choice.

A set of snapshots including the deformation process of elastic gate and elevation of free surface based on SFBI are shown in Fig. 16, with the corresponding experimental photos (Antoci et al., 2007) at the same instants. It can be observed that once the gate is pushed open by the pressure of stored water, the water column flow out immediately. During the stage $t = 0.04 \sim 0.12$ s, the deflection of elastic gate as well as the stress increases gradually, while the level of the free surface decreases. After $t = 0.12$ s, decrease of the deformation and stress of gate can be observed. From the presented figure, the reproduced free surface profiles as well as elastic gate displacements appear to be consistent with those observed in the experiment. MPS-FEM coupled solver has presented a considerable stability in the reproduction of stress field in the elastic gate as well as hydrodynamic pressure field.

Fig. 17 shows the time variation of the water level. Two probes of water height are set behind the gate and at the center of the water column. From the figure, it can be seen that the tendency of the variations is consistent of the result by Antoci et al. (2007). As a consequence, present MPS-FEM coupled method is capable in solving free-surface flow interacting with deformable structures.

4.4. Tank sloshing interacting with an elastic baffle

The second test for MPS-FEM coupled method is the flow in a sloshing tank interacting with an elastic baffle as compared with the experiment result and numerical result by Idelsohn et al. (2008). Two kinds of filling rates are numerically investigated in this paper, the initial configuration is illustrated in Fig. 18. The bottom clamped baffle is immersed in the fluid. The fluid used is sunflower oil with a kinematic viscosity of 50 times (5×10^{-5} m^2/s) that of water at room temperature. The tank is free to roll around the center of bottom of the container, the motion governing equation can be defined as

$$\theta(t) = \theta_0 \sin(\varpi t) \tag{38}$$

The calculation parameters are listed in Table 4. A series of snapshots related to the simulation of the liquid sloshing interacting with deformable baffle are shown in Fig. 19 and Fig. 20. From the figure, the deformation of baffle and elevation of free surface can be observed. The reproduced profiles of the deformed baffle and free surface are coincident with those observed in the experiment. In the Case1, while the fluid flows over the structure, a bubble cavity forms near the top of baffle, which doesn't exist in the experiment. The possible reason for the
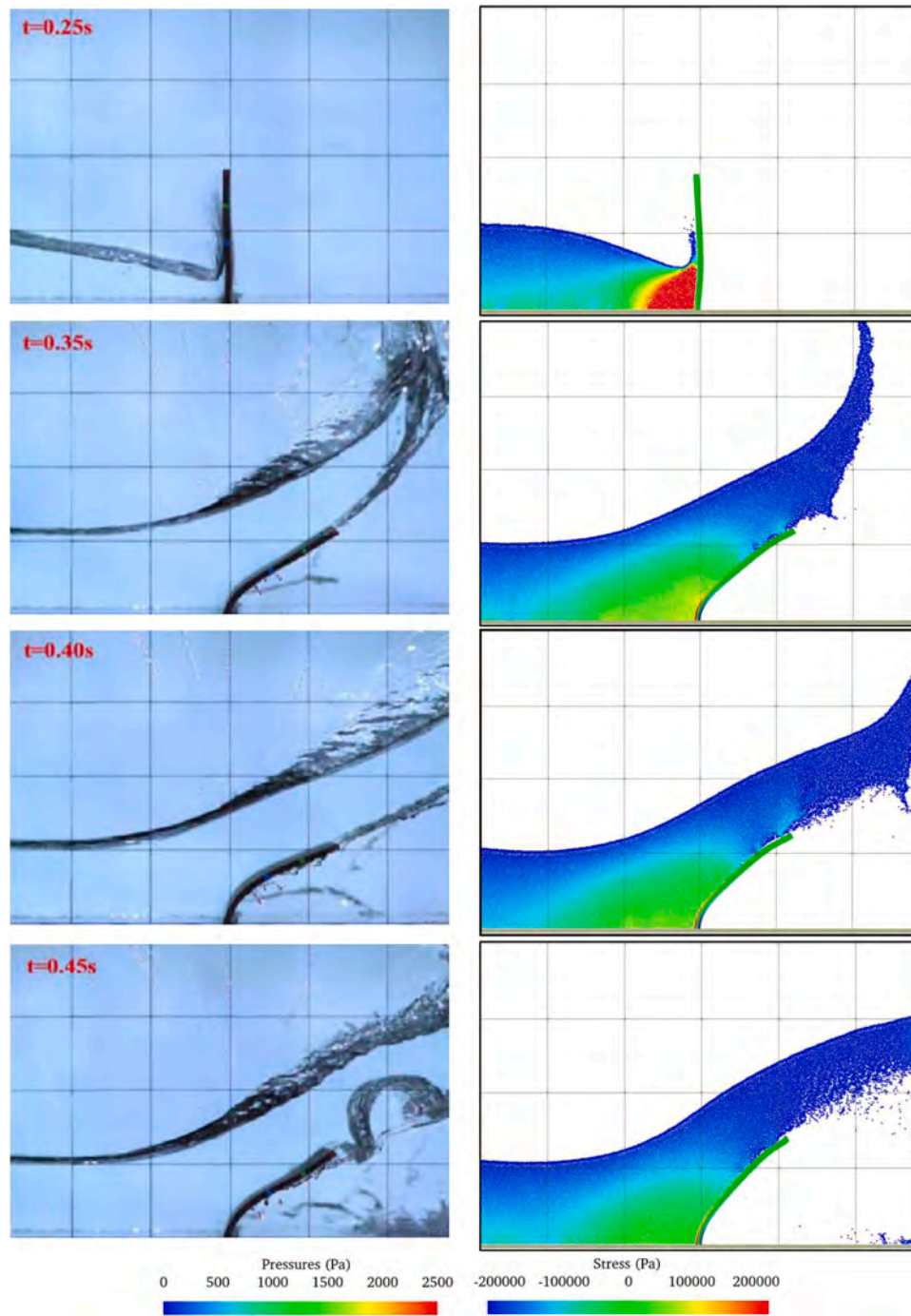
Fig. 26. Free surface profile and deformable structure at typical time steps.

bubble cavity may be the three-dimensional characteristics of real flow, in the experiment the channel is open and air is able to escape. In the Case2, though the interaction between fluid and structure is more intense, hydrodynamic pressure and structure stress are still stable and smooth. Generally, the agreement between the numerical results and the experimental ones are acceptable.

Fig. 21 and Fig. 22 show the time histories of the horizontal displacement of the top of baffle in both cases obtained by MPS-FEM coupled method compared with the experiment data and numerical results from Idelsohn et al. (2008). From the figure of Case1, it can be seen that the trend of numerical curve evolves consistent with the experiment. Though the displacement is a little higher than the experiment result, it agrees with the numerical result from Idelsohn et al.

(2008). In the Case2, both amplitude and period of displacement are in good agreement with experimental data. It can be confirmed that the MPS-FEM coupled method is of effectiveness in solving the periodic and violent interaction between free-surface flow and deformable structures.

4.5. 2D dam-break flow impacting into an elastic plate

The third validation case is dam-break impacting on an elastic obstacle, reproducing the experiment in Liao et al. (2015). As illustrated in Fig. 23, a two-dimensional water tank, with a length of 0.8 m and a height of 0.6 m, is set. The initial water column near the left-hand wall has a width of 0.2 m and a height of 0.3 m. An elastic obstacle is bottom clamped in the water tank, and the distance between the obstacle and
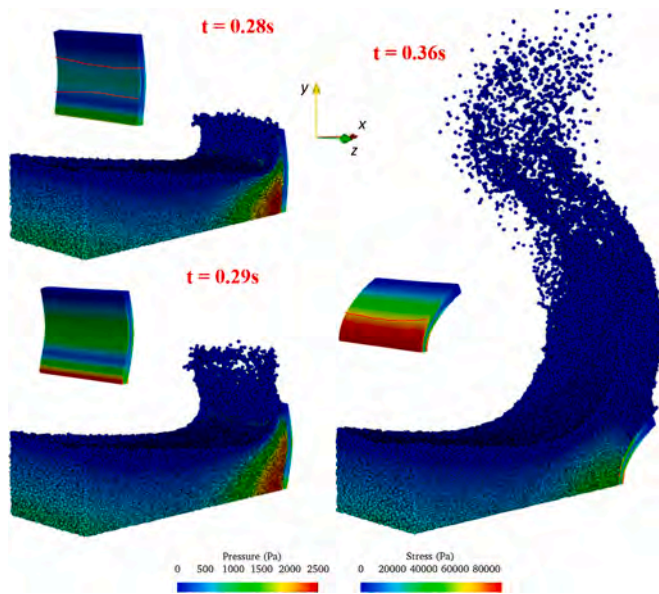
Fig. 27. The simulation of 3D dam breaking flow impacting on an elastic plate.
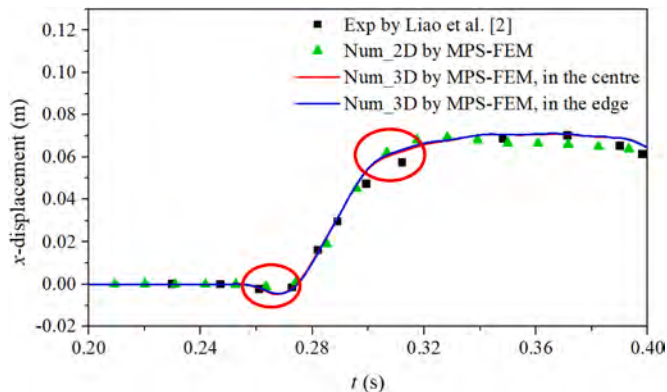

Fig. 28. The *x*-direction deformation of free end of elastic obstacle.

the right-hand side wall is 0.2 m. The elastic obstacle has a thickness of 0.004 m and a height of 0.09 m. The density of the obstacle is 1161.54 kg/m^3, Young's modulus is 3.5×10^6 Pa. The initial particle spacing and grid size are set as $dp = 0.001$ m and $L = 0.002$ m, respectively. SFBI is used for interfacial data interpolation in this section.

It is worth noting that, the accurate considering of the gate motion at the initial stage of the dam breaking test has an essential effect on the formation of the dam-breaking flow and the impact force on the structure. In addition, the gradual lifting-up of the gate slightly delays the collapse of the water column. Therefore, at the initial stage, reasonably good accuracy can be obtained by consideration of the gate motion. To accurately reproduce the gate motion in the present method, the gate is discretized by boundary particles that move upward with the following motion law,

$$H_g(t) = -333.13185t^3 + 81.9191t^2 - 0.31955t \quad (0 < t < 0.1) \tag{39}$$

where $H_g(t)$ denotes the vertical displacement of the gate. The comparision between fitted curve used in the simulation and the experimental data is ploted in Fig. 24. The horizontal displacement of the obstacle is shown in the Fig. 25, compared with the result from Liao et al. (2015). From the figure, it can be seen that at the instant $t = 0.25$ s, the negative displacement can be obviously captured in the numerical simulation. Results show that the main features of phenomenon at the

initial impacting stage are captured by the numerical method, the present MPS-FEM coupled method is capable for simulating the interaction. Especially, a phase error between the experimental data and the numerical result without gate can be observed. The similar phenomenon also appears in Liao et al. (2015). It can be seen that the considering of the gate motion at the initial stage of the dam breaking test has an essential effect. While during the post impact period (after 0.6 s), The rebound of the elastic obstacle in the numerical results is larger than that in the experiment. As Sun et al. (2021b) and Khayyer et al. (2021) pointed out, the possible reason is that the air cavity enclosed by the water is ignored in present paper, which might significantly affect the flow field and the hydrodynamic loading. The modeling of this problem using a multi-phase MPS-FEM model is an ongoing research in the future article. Generally, the agreement between the numerical result and the experiment result is acceptable.

Fig. 26 shows a comparison between experiment and simulation at different time instants. As can be seen from the figure, at the instant $t = 0.25$ s the water head reaches the front side of the elastic obstacle and impacts the structure immediately. Then elastic obstacle produces an obvious deformation under the violent impact. During the stage of $t = 0.25 \sim 0.35$ s, water head climbs upwards along the elastic obstacle, at the same time the displacement of elastic obstacle becomes larger. An upward inclined jet flow along the elastic structure is generated, slamming the right lateral wall. Due to the gravity of jet flow and the diversion effect of the lateral wall, a clockwise roll motion is formed in the right side of the elastic obstacle, and a reverse impact was performed on the elastic structure. It can be observed that obtained deformation of elastic obstacle and free surface flow are in good agreement with experiment. It can be confirmed that MPS-FEM coupled method is of effectiveness in solving two-dimensional FSI problems.

4.6. 3D dam-break flow impacting into an elastic plate

In this section, the proposed MPS-FEM coupled method will be extended to a 3D FSI test. The 3D dam-breaking case is investigated by comparing with the 2D results and the published data (Liao et al., 2015). The numerical configuration is identical with the last section, except that the thickness is set as 0.1 m. To visually observe the 3D flow features, snapshots at certain time instants are depicted in Fig. 27, in which the fluid particles are coloured by pressure and the structure meshes are coloured by the stress. In order to observe the interaction between fluid flow and deformable structure more visually, the flow field between 0.3–0.6 m is presented. It can be found that, the flow in the z direction (thickness direction) presents a slight variation, except for the splashing part. It also can be seen that the stress distribution on the plate is variation in the z direction. Meanwhile, the same 3D characteristics can be captured when observing the horizontal displacements of the elastic plate, as shown in Fig. 28. In the figure, the horizontal displacements of two markers, which are set in the center of the plate and the side of the plate, are compared with the 2D FSI result and experimental data. It can be seen that the two 3D results almost coincide with the 2D result. The 3D characteristics is the most distinct at initial impacting stage, until the plate deflects to the maximum deformation. It can be found that, present MPS-FEM coupled method is capable in simulating 3D FSI problems, and capable to capture the 3D characteristics.

5. Conclusion

This paper presents the partitioned MPS-FEM method in solving the interaction between free surface flows and deformable structure. MPS method is applied to solve the fluid field, while the solid part is modeled with FEM, a weak coupling strategy is implemented to couple two method. Two types of data interpolation techniques applied on the two-dimensional isomerous interface are proposed, including the Shape Function Based Interpolation Technique (SFBI) and Kernel Function Based Interpolation Technique (KFBI). Through the benchmark test of

hydrostatic water column on a thin deformable plate and 2D FSI test of dam-breaking flow interacting with the elastic gate, the precision and convergence of the present interpolation techniques are validated. The outcomes indicated that the data interpolation technique of SFBI is better with its stability and robustness, while the data interpolation technique of KFBI is better with its accuracy when the effective radius is more centered.

Then, through the other two 2D FSI tests, it can be confirmed that the coupled method is of stability in solving the periodic and violent FSI problems. Although, some difference because of ignoring the influence of gas phase still exist. Therefore, in future studies, the present model should be coupled with multi-phase model. Generally, the coupled method can well describe the deformation and the breakup of the free surfaces, and the movement and the deformation of elastic solid objects. In the last test of 3D FSI case of the water impact onto an elastic obstacle, the proposed MPS-FEM coupled method is successfully extended to a 3D model. It means that present MPS-FEM coupled method is effective and capable in simulating 2D/3D FSI problems. In addition, with 3D dam-breaking FSI test, the importance of considering 3D characteristic in some typical FSI problems is highlighted.

In future, our work is to improve the computational efficiency by recourse to graphics processing unit (GPU) computing (Xie et al., 2020) and multi-resolution (Khayyer et al., 2019) scheme. In addition, there are some excellent works worth learning, such as particle generator for arbitrarily complex geometry (Zhu et al., 2021), the elastoplastic deformation of structures (Ming et al., 2016), wave-structure interaction problem (Ni et al., 2019), Fluid-ice-structure interaction problem (Ren et al., 2019; Ni et al., 2020), and coupling hydrodynamic problems (Zhang et al., 2020; Zhuang and Wan, 2021).

Declaration of Competing Interest

The authors declare that they have no known competing financial interests or personal relationships that could have appeared to influence the work reported in this paper.

Acknowledgments

References

Kassiotis, C., Ibrahimbegovic, A., Matthies, H., 2010. Partitioned solution to fluid–structure interaction problem in application to free-surface flows. Eur. J. Mech./B Fluids 29 (6), 510–521.

Liao, K., Hu, C., Sueyoshi, M., 2015. Free surface flow impacting on an elastic structure: experiment versus numerical simulation. Appl. Ocean Res. 50, 192–208.

Idelsohn, S.R., Marti, J., Souto-Iglesias, A., Oñate, E., 2008. Interaction between an elastic structure and free-surface flows: experimental versus numerical comparisons using the PFEM. Comput. Mech. 43 (1), 125–132.

Wick, T., 2013. Solving monolithic fluid-structure interaction problems in arbitrary Lagrangian Eulerian coordinates with the deal.II library. Arch. Numer. Softw. 1 (1), 1–19.

Lucy, L.B., 1977. A numerical approach to the testing of the fission hypothesis. Astron. J. 82, 1013–1024.

Koshizuka, S., Oka, Y., 1996. Moving-particle semi-implicit method for fragmentation of incompressible fluid. Nucl. Sci. Eng. 123 (3), 421–434.

Mitsume, N., Yoshimura, S., Murotani, K., Yamada, T., 2014. Improved MPS-FE fluid-structure interaction coupled method with MPS polygon wall boundary model. Comput. Model. Eng. Sci. 101 (4), 229–247.

Zhang, Y.L., Wan, D.C., 2019. MPS-FEM coupled method for fluid–structure interaction in 3d dam-break flows. Appl. Math. Mech. 16 (02), 879–890.

Zheng, Z.M., Duan, G.T., Mitsume, N., Chen, S., Yoshimura, S., 2020a. A novel ghost cell boundary model for the explicit moving particle simulation method in two dimensions. Comput. Mech. 66 (4), 87–102.

Zheng, Z.M., Duan, G.T., Mitsume, N., Chen, S., Yoshimura, S., 2020b. An explicit MPS/FEM coupling algorithm for three-dimensional fluid-structure interaction analysis. Eng. Anal. Bound. Elem. 121, 192–206.

Yang, Q., Jones, V., McCue, L., 2012. Free-surface flow interactions with deformable structures using an SPH-FEM model. Ocean Eng. 55, 136–147.

Fourey, G., Hermange, C., Touzé, D.Le., Oger, G., 2017. An efficient FSI coupling strategy between smoothed particle hydrodynamics and finite element methods. Comput. Phys. Commun. 217, 66–81.

Hermange, C., Oger, G., Chenadec, Y.L., Touzé, D.L., 2019. A 3D SPH–FE coupling for FSI problems and its application to tire hydroplaning simulations on rough ground. Comput. Methods Appl. Mech. Eng. 355, 558–590.

Sun, Z., Djidjeli, K., Xing, J.T., Cheng, F., 2016. Coupled MPS-modal superposition method for 2D nonlinear fluid-structure interaction problems with free surface. J. Fluids Struct. 61, 295–323.

Sun, Z., Zhang, G.Y., Zong, Z., Djidjeli, K., Xing, J.T., 2019a. Numerical analysis of violent hydroelastic problems based on a mixed MPS-mode superposition method. Ocean Eng. 179, 285–297.

Sun, P.N., Le. Touzé, D., Oger, G., Zhang, A.M., 2021. An accurate FSI-SPH modeling of challenging fluid-structure interaction problems in two and three dimensions. Ocean Eng. 221, 108552.

Zhan, L., Peng, C., Zhang, B., 2019. A stabilized TL–WC SPH approach with GPU acceleration for three-dimensional fluid–structure interaction. J. Fluids Struct. 86, 329–353.

Khayyer, A., Gotoh, H., Falahaty, H., Shimizu, Y., 2018. An enhanced ISPH-SPH coupled method for simulation of incompressible fluid-elastic structure interactions. Comput. Phys. Commun. 232, 139–164.

Khayyer, A., Tsuruta, N., Shimizu, Y., Gotoh, H., 2019. Multi-resolution MPS for incompressible fluid-elastic structure interactions in ocean engineering. Appl. Ocean Res. 82, 397–414.

Zhang, C., Rezavand, M., Hu, X.Y., 2021. A multi-resolution SPH method for fluid-structure interactions. J. Comp. Phys. 429, 110028.

Long, T., Huang, C., Hu, D., Liu, M.B., 2021. Coupling edge-based smoothed finite element method with smoothed particle hydrodynamics for fluid structure interaction problems. Ocean Eng. 225, 108772.

Khayyer, A., Shimizu, Y., Gotoh, H., Nagashima, K., 2021a. A coupled Incompressible SPH-Hamiltonian SPH solver for hydroelastic FSI corresponding to composite structures. Appl. Math. Model. 94, 242–271.

Walhorn, E., Kolke, A., Hübner, B., Dinkler, D., 2005. Fluid–structure coupling within a monolithic model involving free surface flows. Comput. Struct. 83 (25–26), 2100–2111.

Dettmer, W.G., Perić, D., 2007. A fully implicit computational strategy for strongly coupled fluid–solid interaction. Arch. Comput. Meth. Eng. 14 (3), 205–247.

Farhat, C., Lesoinne, M., 2000. Two efficient staggered algorithms for the serial and parallel solution of three-dimensional nonlinear transient aeroelastic problems. Comput. Methods Appl. Mech. Eng. 182 (3–4), 499–515.

Tallec, P.L., Mouro, J., 2001. Fluid structure interaction with large structural displacements. Comput. Methods Appl. Mech. Eng. 190 (24–25), 3039–3067.

Zhang, Y.L., Wan, D.C., 2018. MPS-FEM coupled method for sloshing flows in an elastic tank. Ocean Eng. 153, 416–427.

Rao, C.P., Zhang, Y.L., Wan, D.C., 2017. Numerical simulation of the solitary wave interacting with an elastic structure using MPS-FEM coupled method. J. Mar. Sci. Appl. 16, 395–404.

Rao, C.P., Wan, D.C., 2018. Numerical study of the wave-induced slamming force on the elastic plate based on MPS-FEM coupled method. J. Hydrodyn. Ser. B (Engl. Ed.) 30 (1), 70–78.

Zhang, G.Y., Chen, X., Wan, D.C., 2019. MPS-FEM coupled method for study of wave-structure interaction. J. Mar. Sci. Appl. 18 (4), 387–399.

Gao, W., Matsunaga, T., Duan, G.T., Koshizuka, S., 2021. A coupled 3D isogeometric/least-square MPS approach for modelling fluid–structure interactions. Comput. Methods Appl. Mech. Eng. 373, 113538.

Antoci, C., Gallati, M., Sibilla, S., 2007. Numerical Simulation of Fluid–structure Interaction by SPH. Comput. Struct. 85 (11), 879–890.

Khayyer, A., Gotoh, H., 2011. Enhancement of stability and accuracy of the moving particle semi-implicit method. J. Comput. Phys. 230, 3093–3118.

Tamai, T., Koshizuka, S., 2014. Least squares moving particle semi-implicit method. Computat. Partic. Mech. 1, 277–305.

Khayyer, A., Gotoh, H., Shimizu, Y., Gotoh, Y.K., 2017a. On enhancement of energy conservation properties of projection-based particle methods. Eur. J. Mech. B. Fluids 66, 20–37.

Lind, S.J., Xu, R., Stansby, P.K., Rogers, B.D., 2012. Incompressible smoothed particle hydrodynamics for free-surface flows: a generalised diffusion-based algorithm for stability and validations for impulsive flows and propagating waves. J. Comput. Phys. 231 (4), 1499–1523.

Duan, G.T., Yamaji, A., Koshizuka, S., Chen, B., 2019. The truncation and stabilization error in multiphase moving particle semi-implicit method based on corrective matrix: which is dominant? Comput. Fluids 190, 254–273.

Khayyer, A., Gotoh, H., Shimizu, Y., 2017b. Comparative study on accuracy and conservation properties of two particle regularization schemes and proposal of an optimized particle shifting scheme in ISPH context. J. Comput. Phys. 332, 236–256.

Tsuruta, N., Khayyer, A., Gotoh, H., 2013. A short note on dynamic stabilization of moving particle semi-implicit method. Comput. Fluids 82, 158–164.

Lee, B.H., Park, J.C., Kim, M.H., Hwang, S.C., 2011. Step-by-step improvement of MPS method in simulating violent free-surface motions and impact-loads. Comput. Methods Appl. Mech. Eng. 200 (9–12), 1113–1125.

Zhang, Y.X., Wan, D.C., 2012. Apply MPS method to simulate liquid sloshing in LNG tank. In: Proceedings of 22nd International Offshore and Polar Engineering Conference. Rhodes, Greece, pp. 381–391.

Zhang, Y.X., Wan, D.C., Hino, T., 2014. Comparative study of MPS method and level-set method for sloshing flows. J. Hydrodyn. Ser. B (Engl. Ed.) 26 (4), 577–585.

Tang, Z.Y., Zhang, Y.L., Wan, D.C., 2016a. Numerical simulation of 3D free surface flows by overlapping MPS. J. Hydrodyn. Ser. B (Engl. Ed.) 28 (2), 306–312.

Tang, Z.Y., Zhang, Y.L., Wan, D.C., 2016b. Multi-resolution MPS method for free surface flows. Int. J. Comput. Methods 13 (4), 1641018.

Tanaka, M., Masunaga, T., 2010. Stabilization and smoothing of pressure in MPS method by quasi-compressibility. J. Comput. Phys. 229 (11), 4279–4290.

Khayyer, A., Gotoh, H., Shao, S.D., 2009. Enhanced predictions of wave impact pressure by improved incompressible SPH methods. Appl. Ocean Res. 31 (2), 111–131.

Belytschko, T., Liu, W.K., Moran, B., Elkhodary, K., 2014. Nonlinear Finite Elements for Continua and Structures. John Wiley & Sons Inc.

Newmark, N.M., 1959. A method of computation for structural dynamics. J. Eng. Mech. Div. 85 (3), 67–94.

Hsiao, K.M., Lin, J.Y., Lin, W.Y., 1999. A consistent corotational finite element formulation for geometrically nonlinear dynamic analysis of 3-D beams. Comput. Methods Appl. Mech. Eng. 169, 1–18.

Landau, L.D., Lifshitz, E.M., 1970. Theory of elasticity. In: Course of Theoretical Physics, 7. Pergamon Press, Oxford.

Gray, J.P., Monaghan, J.J., Swift, R.P., 2001. SPH elastic dynamics. Comput. Methods Appl. Mech. Eng. 190 (49), 6641–6662.

Sun, P.N., Touzé, D.Le, Zhang, A.M., 2019b. Study of a complex fluid-structure dam-breaking benchmark problem using a multi-phase SPH method with APR. Eng. Anal. Bound. Elem. 104, 240–258.

Khayyer, A., Shimizu, Y., Gotoh, H., Hattori, S., 2021b. Multi-resolution ISPH-SPH for accurate and efficient simulation of hydroelastic fluid-structure interactions in ocean engineering. Ocean. Eng. 226, 108652.

Xie, F.Z., Zhao, W.W., Wan, D.C., 2020. CFD simulations of three-dimensional violent sloshing flows in tanks based on MPS and GPU. J. Hydrodyn. Ser. B (Engl. Ed.) 32 (5), 672–683.

Zhu, Y., Zhang, C., Yu, Y., Hu, X., 2021. A CAD-compatible body-fitted particle generator for arbitrarily complex geometry and its application to wave-structure interaction. J. Hydrodyn. Ser. B (Engl. Ed.) 33 (2), 195–206.

Ming, F.R., Zhang, A.M., Xue, Y.Z., Wang, S.P., 2016. Damage characteristics of ship structures subjected to shockwaves of underwater contact explosions. Ocean Eng. 117, 359–382.

Ni, X.Y., Feng, W.B., Huang, S.C., Hu, Z.J., Liu, Y., 2019. An SPH wave-current flume using open boundary conditions. J. Hydrodyn. Ser. B (Engl. Ed.) 32 (3), 536–547.

Ren, D., Park, J.C., Hwang, S.C., Jeong, S.Y., Kim, H.S., 2019. Failure simulation of ice beam using a fully Lagrangian particle method. Int. J. Naval Arch. Ocean Eng. 11 (2), 639–647.

Ni, B.Y., Han, D.F., Di, S.C., Xue, Y.Z., 2020. On the development of ice-water-structure interaction. J. Hydrodyn. Ser. B (Engl. Ed.) 32 (18).

Zhang, X.S., Wang, J.H., Wan, D.C., 2020. Numerical techniques for coupling hydrodynamic problems in ship and ocean engineering. J. Hydrodyn. Ser. B (Engl. Ed.) 2, 212–233.

Zhuang, Y., Wan, D.C., 2021. Parametric study of a new HOS-CFD coupling method. J. Hydrodyn. Ser. B (Engl. Ed.) 33 (1), 43–54.